



IRPO: Boosting Image Restoration via Post-training GRPO

Haoxuan Xu^{1*} Yi Liu^{2*} Boyuan Jiang³ Jinlong Peng³ Donghao Luo³
Xiaobin Hu^{4†} Shuicheng Yan⁴ Haoang Li¹

¹The Hong Kong University of Science and Technology (Guangzhou) ²Tsinghua University

³Tencent YouTu Lab ⁴National University of Singapore

Abstract

Recent advances in post-training paradigms have achieved remarkable success in high-level generation tasks, yet their potential for low-level vision remains rarely explored. Existing image restoration (IR) methods rely on pixel-level hard-fitting to ground-truth images, struggling with over-smoothing and poor generalization. To address these limitations, we propose IRPO, a low-level GRPO-based post-training paradigm that systematically explores both data formulation and reward modeling. We first explore a data formulation principle for low-level post-training paradigm, in which selecting underperforming samples from the pre-training stage yields optimal performance and improved efficiency. Furthermore, we model a reward-level criteria system that balances objective accuracy and human perceptual preference through three complementary components: a General Reward for structural fidelity, an Expert Reward leveraging Qwen-VL for perceptual alignment, and a Restoration Reward for task-specific low-level quality. Comprehensive experiments on six in-domain and five out-of-domain (OOD) low-level benchmarks demonstrate that IRPO achieves state-of-the-art results across diverse degradation types, surpassing the AdaIR baseline by 0.83 dB on in-domain tasks and 3.43 dB on OOD settings. Our code can be shown in <https://github.com/HaoxuanXU1024/IRPO>.

1. Introduction

In recent years, the development of the pre-training and post-training paradigm [84] has driven remarkable progress in generative tasks such as image generation [38, 44], video generation [26, 35, 40], and 3D generation [22]. Fundamentally, the post-training paradigm refines a pre-trained model’s distribution modeling capability through a small amount of high-quality data and reward signals [30]. In generative modeling, post-training paradigm serves as an alignment phase [39], transforming a model from merely gener-

*Haoxuan Xu and Yi Liu are co-first authors

†Corresponding authors.

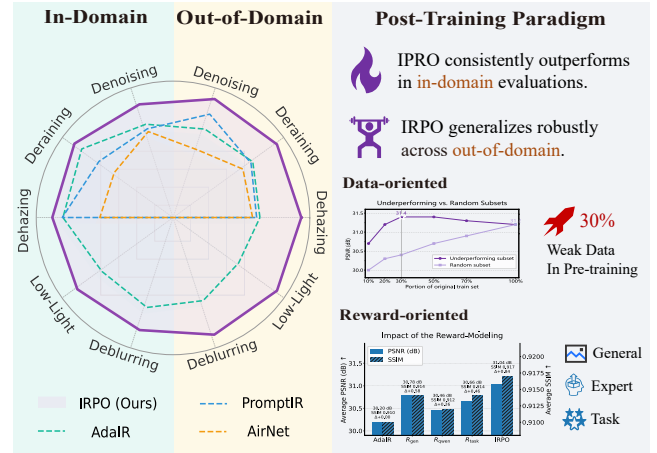


Figure 1. An overview of our IRPO post-training paradigm and its performance. (Left) Radar plot comparing average PSNR, showing IRPO achieves SOTA In-Domain performance and vastly superior Out-of-Domain generalization. (Right) The two pillars of our paradigm: Data-oriented, which finds that training on the 30% Weak Data (underperforming subset) is optimal, and Reward-oriented showing the benefit of our reward components.

ating plausible outputs to producing results that more faithfully reflect human intent [16]. The success of post-training in high-level generative tasks [56] naturally suggests its potential for low-level tasks as well. While high-level tasks focus on semantic richness in the generated outputs, low-level tasks also require a balance between physical accuracy and perceptual naturalness [58, 82]. This insight reveals that post-training can serve as a key mechanism for human-aligned restoration in low-level vision tasks, shifting the optimization focus from pixel-level reconstruction toward perceptually coherent restoration. Consequently, a valuable research problem is to effectively and efficiently adapt the post-training paradigm to low-level image restoration (IR) tasks.

Existing training strategies for low-level IR models can generally be categorized into three paradigms: **1) Single-stage training:** which trains a restoration network end-to-

end using all data in one pass, directly mapping degraded inputs to clean outputs [25]. Although simple and efficient, it often struggles to handle complex degradations due to limited representation adaptability. **2) Progressive training:** which is trained in multiple sequential stages [43, 72], typically moving from low-quality to high-quality restoration [74]. While this approach improves stability and can yield higher-quality results, it requires handcrafted curriculum scheduling and fine-tuning of intermediate objectives, making it harder to generalize. **3) Task-specific fine-tuning:** which further fine-tunes on a specific dataset, yielding high accuracy on the target domain [42, 62, 66]. However, it requires large amounts of task-specific labeled data, incurs high computational cost for every new task, and sacrifices generalization across multiple degradation types. Overall, these training paradigms follow a deterministic supervision framework [65] that hard-fits static objectives. Such rigid, hard-fitting approach is fundamentally misaligned with human perceptual preferences [5], which limits the model’s generalization and adaptability to real-world degradations.

The limitation of hard-fitting supervision training calls for a novel fine-tuning optimization paradigm. The human-like “understanding” process is essentially a complex, non-differentiable objective that aligns with perceptual quality and human preference, rather than simple pixel distance. As a post-training paradigm, Reinforcement Learning (RL), particularly Group Relative Policy Optimization (GRPO) [57], is perfectly suited for this challenge due to its ability to effectively optimize complex and arbitrary reward signals [68]. This motivates us to re-frame the IR post-training process as a policy optimization problem. To achieve this goal, the target post-training paradigm for low-level IR tasks we seek must possess two properties: **1) Data Formulation**, unlike high-level tasks where multiple outputs can be ranked according to human preference, IR tasks lack an intuitive and consistent criterion to determine which restoration result is superior. Moreover, obtaining high-quality paired training data of degraded and ground-truth images for low-level tasks is expensive and time-consuming [31], while synthetic degradations often fail to represent real-world scenarios. **2) Reward Modeling**, conventional IR models are typically optimized using deterministic supervision training [28], which poorly reflect human perceptual judgment. Such objectives fail to adaptively address different types of degradations, resulting in weak and ambiguous reward signals in low-level image restoration tasks.

To address these issues, this paper proposes an **Image Restoration** framework powered by a systematic GRPO-based post-training paradigm (IRPO), consisting of data-oriented supervision and reward-oriented optimization paradigm (Figure 1). We first explore the data formulation for low-level post-training paradigm through extensive random sampling and performance-based selection, formu-

lating a simple yet effective data-oriented principle: post-training exclusively on the 30% underperforming samples from the pre-training stage yields the optimal balance of performance and efficiency. Next, in low-level tasks, there exist substantial differences across task types, and the optimization objectives must satisfy both objective metrics and human subjective perception. To this end, we build a task-aware, human-aligned reward system with three parts: (1) General Reward to ensure a well-formatted and structured restoration process. (2) Expert Reward: using QwenVL for multi-faceted judgments of quality, realism, and consistency; and (3) Restoration Reward to specifically assesses the extent of low-level processing. Finally, motivated by all-in-one IR [10, 49], we evaluate GRPO post-training under mixed-degradation training, highlighting its adaptability to real-world scenarios.

In summary, our contributions are as follows:

- To the best of our knowledge, this is the first low-level GRPO-based post-training paradigm that systematically explores both data formulation and reward modeling, laying the foundation for more generalizable and accurate image restoration.
- We advance the low-level post-training paradigm by modeling reward-level criteria and exploring a simple yet effective performance-based data-oriented principle, comprehensively guiding the restoration process to generate more realistic images.
- We further explore the adaptability of the GRPO post-training paradigm under all-in-one mixed training settings, showing superior performance even without relying on prior degradation information.
- We evaluate our method on six in-domain and five out-of-domain (OOD) low-level benchmarks, demonstrating that our post-training paradigm achieves state-of-the-art performance against existing IR training paradigm and superior robustness on generalizable scenes.

2. Related Work

2.1. Low Level Training Paradigm

Training strategies for low-level vision largely fall into three paradigms: 1) Single-stage Training. Models are trained end-to-end to map degraded inputs to clean outputs. Early CNN-based restorers such as DnCNN [78] and SRCNN [12], and later transformer variants like SwinIR [36] and Restormer [73], demonstrate that strong architectures can learn the restoration mapping efficiently. 2) Progressive Training. Outputs are refined from coarse to fine via multi-stage designs like MPRNet [72] and MIRNet [74], or progressive learning strategies such as Diff-Mamba [43] that improve stability and final accuracy. However, this strategy introduces significant complexity, requiring carefully designed intermediate supervision and being susceptible to error propagation across stages, which can hinder general-

ization. 3) Task-specific Fine-tuning. Broadly pre-trained models are adapted to specific domains[71], *e.g.*, transferring synthetic denoisers like DnCNN [78] to real camera noise in CBDNet [18], customizing ESRGAN [63] to anime styles in APISR [33] or facial details [19, 20], or specializing video restorers like VRT [37] for motion blur or compression artifacts [42]. While accurate on-target, this requires extra labeled data per task and often induces catastrophic forgetting across degradations.

While existing methods employ diverse training strategies to optimize pixel-level metrics, they still rely on hard fitting to the training set for an understanding-generative problem formulation, which results in poor restoration performance on OOD test sets [5, 28]. We explore a systematic GRPO-based post-training paradigm for low-level tasks, consisting of data-oriented supervision and reward-oriented optimization paradigm, demonstrating exceptional robustness and generalization in adapting to diverse real-world scenarios.

2.2. Reinforcement Learning

Recent progress in RL has markedly boosted LLMs’ reasoning by post-training that elicits deliberate, stepwise thinking [53, 60]. OpenAI’s o1 [24] exemplifies how RL strengthens structured reasoning. Unlike RLHF [4] with heavy value networks, GRPO [57] uses intra-group relative advantages for stable, efficient learning. Building on this, DeepSeek-R1 [17] combines rule-based rewards with GRPO to encourage thorough reasoning before answers. Owing to its efficiency and generality, GRPO has quickly extended beyond NLP to multimodal generation [9, 68, 77], high-level image/video generation [35, 44], speech understanding [29], and decision-making [50, 70], achieving strong results across high-level domains.

Despite these advances, GRPO-style post-training is largely unexplored for low-level restoration due to scarce data [31] and challenging reward design [5]. As in high-level tasks, low-level restoration must balance physical fidelity with perceptual naturalness [58]. We therefore investigate a low-level GRPO paradigm that systematically addresses data formulation and reward modeling, aiming for more generalizable and accurate image restoration.

3. Method

3.1. A Post-Training Paradigm for Low-Level Vision

The prevailing paradigm for training image restoration models is monolithic, end-to-end supervision. This approach has two main limitations. First, by treating all data points equally, it struggles to fix complex, long-tail degradations, which limits model robustness. Second, it relies on simple deterministic supervision framework, with a static pixel-level objective that is often misaligned with human

perceptual preferences (like texture and realism) and leads to overly smooth results.

To overcome these issues, we re-frame the process from single-stage training to a focused post-training phase. We introduce a new post-training paradigm designed to enhance both robustness and perceptual quality. As illustrated in Figure 2, our approach consists of two main pillars: Data-Oriented Supervision, which rectifies the model’s failures on underperformance data (Sec. 3.2), and Reward-Oriented Optimization, which optimizes for complex perceptual rewards (Sec. 3.3).

3.2. Pillar 1: Data-Oriented Supervision

Exploration on Data Curation. We first investigate how data selection impacts post-training. Our exploration reveals that naive fine-tuning on the full training dataset, or even on randomly sampled subsets, yields only marginal gains (as shown in Figure 5). This lead us to a critical insight: post-training is maximally effective only when it focuses on the hard-tail of the data distribution—the samples that the pre-trained model failed to learn.

Based on this exploration, we utilize a specific subset $\mathcal{D}_{\text{hard}} \subset \mathcal{D}$, which contains the worst-performing 30% of the training data. Our Data-Oriented pillar concentrates all supervisory signals exclusively on this set.

Differentiable Supervision on $\mathcal{D}_{\text{hard}}$. For this hard-data subset, we optimize the restoration backbone \mathcal{F} using two differentiable, data-driven losses. First, we identify the best-scoring sample y_{g^*} (where $g^* = \arg \max_i r_i$ via our reward model) from a group of G stochastic rollouts (see Sec. 3.3). We then impose a standard ℓ_1 loss:

$$\mathcal{L}_{\text{sup}} = \ell_1(y_{g^*}, \hat{y}), \quad (1)$$

where \hat{y} is the ground-truth clean image. This provides a strong gradient signal to the backbone.

Second, to ensure stability, we compute a deterministic output y_{det} (using the mean of the Beta policy distributions) and enforce a consistency objective:

$$\mathcal{L}_{\text{cons}} = \ell_1(y_{g^*}, y_{\text{det}}), \quad (2)$$

This loss anchors the stochastic policy’s best output to its stable, deterministic counterpart.

3.3. Pillar 2: Reward-Oriented Optimization

The supervised losses in Pillar 1 can only optimize for pixel-level fidelity (L1). To align our model with complex human preferences, we must incorporate non-differentiable reward signals. Our reward function (detailed below) includes metrics crucial for perception but unusable as a direct loss, such as R_{qwen} (worked as a expert judge) and R_{aes} (aesthetic score, a component of R_{gen}). Since gradients cannot be backpropagated through these scores, we *must* adopt a policy gradient method (GRPO) to optimize our policy π_θ using these rewards.

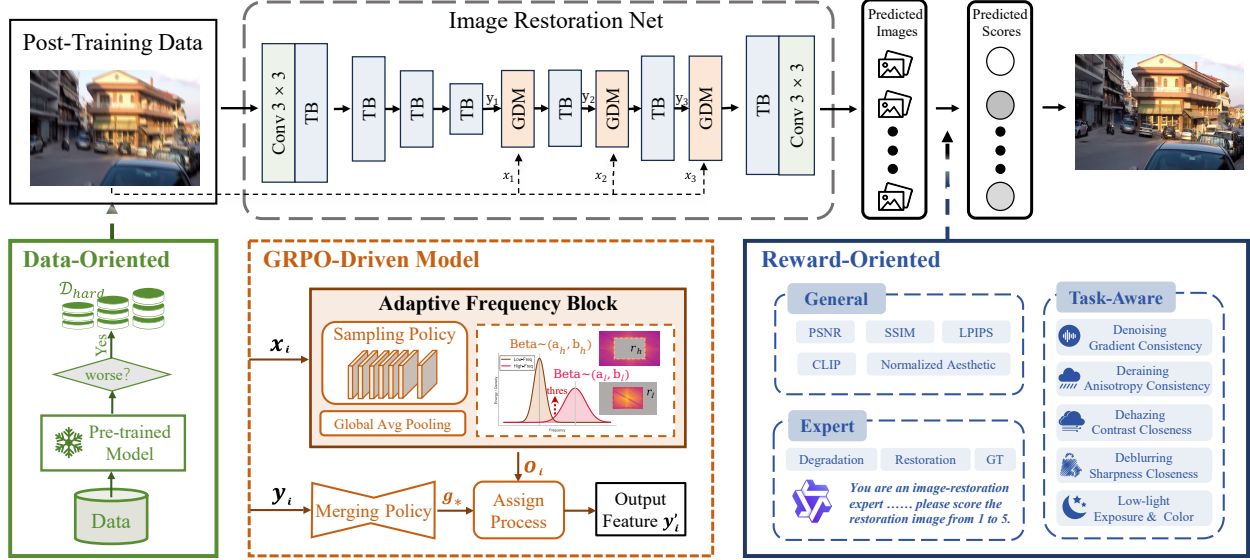


Figure 2. The overview of our proposed post-training paradigm, visually structured around its two pillars. Pillar 1 (Data-Oriented, left): A pre-trained model evaluates the full dataset to curate $\mathcal{D}_{\text{hard}}$, which serves as the post-training data. Pillar 2 (Reward-Oriented, right): A multi-component reward model (General, Expert, Task-Aware) provides signals to train the policy (π_θ). The Image Restoration Net restores underperforming data $\mathcal{D}_{\text{hard}}$, including some TB (Transformer Block) and GDM (GRPO-Driven Model, bottom-middle).

Reward Modeling. We design a composite reward signal based on three core principles:

$$R(y_{g^*}, \hat{y}) = \lambda_{\text{gen}} R_{\text{gen}} + \lambda_{\text{qwen}} R_{\text{qwen}} + \lambda_{\text{task}} R_{\text{task}}, \quad (3)$$

where y_{g^*} is the restored output, \hat{y} is the ground-truth, and $\lambda_{\text{gen}}, \lambda_{\text{qwen}}, \lambda_{\text{task}}$ are fixed balancing hyperparameters.

- **Generic Quality** (R_{gen}): A broad-spectrum reward aggregating metrics like LPIPS, CLIP similarity, and Aesthetic score, alongside PSNR and SSIM, to ensure foundational fidelity.
- **Expert Preference** (R_{qwen}): An expert Qwen-VL model that provides a high-level (1-5) score for perceptual plausibility, steering the model towards human preference.
- **Task-Aware Reward** (R_{task}): A specialized heuristic reward (e.g., gradient consistency for denoising) that guides the policy to fix the correct attributes for each specific degradation task.

All detailed formulas and rewards are seen in Appendix B.

Policy Parametrization. To be optimized by RL, we adapt the deterministic AdaIR [10] backbone \mathcal{F} into a stochastic policy π_θ . We design a GRPO-Driven Model (GDM) adding lightweight policy heads to adapt to the stochastic characteristics of GRPO (see Figure 2, bottom-middle), exposing four continuous controls (r_h, r_l, g_f, g_o) as the action a . A policy head π_θ outputs Beta distribution parameters $(\alpha, \beta) \in \mathbb{R}_+^4$ for these controls:

$$a_k \sim \text{Beta}(\alpha_k, \beta_k), \quad \text{for } k \in \{h, l, f, o\}. \quad (4)$$

The joint log-probability $\log \pi_\theta(a | x)$ has a closed form. The sampled action $a_i = (r_h, r_l, g_f, g_o)_i$ is obtained from

the GDM modules. We design the Adaptive Frequency Block to extract high and low frequency (r_h, r_l) from input image x_i . The first two actions, $(r_h, r_l)_i$, obtained from Sampling Policy, control the frequency-domain mask used to generate an intermediate output feature O_i . The final two actions, $(g_f, g_o)_i$, obtained from Merging Policy, dynamically fuse this new feature O_i with the original Latent Feature y_i in Assign Process:

$$y'_i = g_{f,i} \cdot y_i + g_{o,i} \cdot O_i, \quad \text{for } i \in \{1, 2, 3\}, \quad (5)$$

where y'_i is the new feature passed to the next decoder block. This stochastic modulation results in the final restored candidate $y_g = \mathcal{F}(x)$. We sample G such actions for each input image x . (See Appendix D for full implementation).

Optimization Objective. To optimize the policy π_θ using our non-differentiable reward R , we employ the GRPO framework. We provide a detailed background on GRPO in Appendix A. In brief, GRPO is a policy gradient algorithm that constructs a *group-normalized* relative advantage A_i from a group of G rollouts. This A_i is then used in a clipped, PPO-like surrogate objective to update the policy. Our full RL objective, \mathcal{L}_{RL} , is:

$$\begin{aligned} \mathcal{L}_{\text{RL}}(\theta) = & - \frac{1}{G} \sum_{i=1}^G \min \left(\rho_i(\theta) A_i, \text{clip}(\rho_i(\theta), 1 - \epsilon, 1 + \epsilon) A_i \right) \\ & + \beta \hat{\mathcal{D}}_{\text{KL}}(\pi_\theta \| \pi_{\text{ref}}) - \tau \mathcal{H}(\pi_\theta), \end{aligned} \quad (6)$$

where $\rho_i(\theta)$ is the likelihood ratio, A_i is the group-normalized advantage, β controls the KL penalty, τ is the

Table 1. Single-task comparisons for dehazing (a), deraining (b), and denoising (c). For this setting, each model was trained separately on its respective dataset. IRPO achieves new SOTA performance across all three benchmarks. All metrics shown are PSNR/SSIM.

(a) Dehaze (SOTS)			(b) Derain (Rain100L)			(c) Denoise (Urban100+BSD68)							
Method	PSNR	SSIM	Method	PSNR	SSIM	Method	Urban100			BSD68			Average
							$\sigma = 15$	$\sigma = 25$	$\sigma = 50$	$\sigma = 15$	$\sigma = 25$	$\sigma = 50$	
DehazeNet [6]	22.46	0.851	DIDMDN [75]	23.79	0.773	CBM3D [11]	33.93/0.941	31.36/0.909	27.93/0.840	33.50/0.922	30.69/0.868	27.36/0.763	30.80/0.874
MSCNN [54]	22.06	0.908	UMR [69]	32.39	0.921	DnCNN [78]	32.98/0.931	30.81/0.902	27.59/0.833	33.89/0.930	31.23/0.883	27.92/0.789	30.74/0.878
EPDN [51]	22.57	0.863	MSPFN [27]	33.50	0.948	IRCNN [79]	27.59/0.833	31.20/0.909	27.70/0.840	33.87/0.929	31.18/0.882	27.88/0.790	29.90/0.864
FDGAN [13]	23.15	0.921	LPNet [15]	33.61	0.958	FFDNet [80]	33.83/0.942	31.40/0.912	28.05/0.848	33.87/0.929	31.21/0.882	27.96/0.789	31.05/0.884
AirNet [33]	23.18	0.900	AirNet [33]	34.90	0.977	BRDNet [59]	34.42/0.946	31.99/0.919	28.56/0.858	34.10/0.929	31.43/0.885	28.16/0.794	31.44/0.889
Restormer [73]	30.87	0.969	Restormer [73]	36.74	0.978	AirNet [33]	34.40/0.949	32.10/0.924	28.88/0.871	34.14/0.936	31.48/0.893	28.23/0.806	31.54/0.897
PromptIR [49]	31.31	0.973	PromptIR [49]	37.04	0.979	PromptIR [49]	34.77/0.952	32.49/0.929	29.39/0.881	34.34/0.938	31.71/0.897	28.49/0.813	31.87/0.902
AdaIR [10]	31.80	0.981	AdaIR [10]	38.90	0.985	Adair [10]	34.96/0.953	32.74/0.931	29.70/0.885	34.36/0.938	31.72/0.897	28.49/0.813	32.00/0.903
IRPO (Ours)	32.31	0.983	IRPO (Ours)	39.38	0.988	IRPO (Ours)	35.08/0.954	32.95/0.933	30.07/0.888	34.45/0.940	31.91/0.899	28.71/0.815	32.19/0.905

Table 2. Comparisons for five-degradation all-in-one restoration. Denoising results are reported for the noise level $\sigma = 25$. The top super-row methods denote the general image restoration approaches, and the rest are specialized all-in-one approaches. Our model attains a remarkable average gain of 0.83 dB over AdaIR [10].

Method	Dehazing on SOTS	Deraining on Rain100L	Denoising on BSD68	Deblurring on GoPro	Low-Light on LOL	Average
NAFNet [8]	25.23/0.939	35.56/0.967	31.02/0.883	26.53/0.808	20.49/0.809	27.76/0.881
HINet [7]	24.74/0.937	35.67/0.969	31.00/0.881	26.12/0.788	19.47/0.800	27.40/0.875
MPRNet [72]	24.27/0.937	38.16/0.981	31.35/0.889	26.87/0.823	20.84/0.824	28.27/0.890
DGUNet [47]	24.78/0.940	36.62/0.971	31.10/0.883	27.25/0.837	21.87/0.823	28.32/0.891
MIRNetV2 [74]	24.03/0.927	33.89/0.954	30.97/0.881	26.30/0.799	21.52/0.815	27.34/0.875
SwinIR [36]	21.50/0.891	30.78/0.923	30.59/0.868	24.52/0.773	17.81/0.723	25.04/0.835
Restormer [73]	24.09/0.927	34.81/0.962	31.49/0.884	27.22/0.829	20.41/0.806	27.60/0.881
DL [14]	20.54/0.826	21.96/0.762	23.09/0.745	19.86/0.672	19.83/0.712	21.05/0.743
Transweather [61]	21.32/0.885	29.43/0.905	29.00/0.841	25.12/0.757	21.21/0.792	25.22/0.836
TAPE [41]	22.16/0.861	29.67/0.904	30.18/0.855	24.47/0.763	18.97/0.621	25.09/0.801
AirNet [33]	21.04/0.884	32.98/0.951	30.91/0.882	24.35/0.781	18.18/0.735	25.49/0.846
IDR [76]	25.24/0.943	35.63/0.965	31.60/0.887	27.87/0.846	21.34/0.826	28.34/0.893
AdaIR [10]	30.53/0.978	38.02/0.981	31.35/0.889	28.12/0.858	23.00/0.845	30.20/0.910
IRPO (Ours)	31.36/0.982	38.72/0.987	32.13/0.896	28.89/0.863	24.08/0.858	31.03/0.917

entropy bonus, π_{ref} denotes the reference policy for KL regularization, and π_{θ} is the policy being optimized.

3.4. Final Hybrid Objective

Our final objective combines the pillars. We jointly optimize the policy π_{θ} (via \mathcal{L}_{RL} from Pillar 2) and the backbone \mathcal{F} (via \mathcal{L}_{sup} and $\mathcal{L}_{\text{cons}}$ from Pillar 1). All computations are performed on our curated hard-data subset $\mathcal{D}_{\text{hard}}$:

$$\mathcal{L}_{\text{total}}(\theta) = \mathbb{E}_{(x,g) \sim \mathcal{D}_{\text{hard}}} [\mathcal{L}_{\text{RL}}(\theta) + \lambda_{\text{sup}} \mathcal{L}_{\text{sup}} + \lambda_{\text{cons}} \mathcal{L}_{\text{cons}}], \quad (7)$$

where λ_{sup} and λ_{cons} are weights with linear annealing schedules (see Implementation Details in Appendix C).

4. Experiment

4.1. Experimental Setup

Datasets. In preparing datasets for training and testing, we closely follow prior state-of-the-art works [10, 33, 49].

In-Domain (ID) Datasets. Our training and evaluation cover five restoration tasks. For image dehazing, we use SOTS [32] dataset that comprises 72,135 training images and 500 testing images. For image deraining, we utilize the Rain100L [67] dataset, which contains 200 clean-rainy image pairs for training and 100 pairs for testing. For image deblurring, we use the GoPro dataset [48], providing 2,103 training pairs and 1,111 testing pairs. For low-light enhancement, we use the LOL dataset [64], which consists of 485 training pairs and 15 test pairs. For image denoising, we combine images of BSD400 [2] and WED [45] datasets for model training; the BSD400 encompasses 400 training images, while the WED dataset consists of 4,744 images. Based on these clean images, we generate their corresponding noisy versions by adding Gaussian noise with varying levels ($\sigma \in \{15, 25, 50\}$). Denoising task evaluation is performed on the BSD68 [46] and Urban100 [21] datasets.

Out-of-Domain (OOD) Datasets. To evaluate the generalization capabilities of our model, we test it on five

Table 3. Quantitative comparison on the out-of-domain (OOD) real-world test set, including RRSID [83] for dehazing, GT-Rain [3] for deraining, SIDD [1] for denoising, ReLoBlur [34] for deblurring, and LoLi-Street [23] for low-light enhancement. Our IRPO demonstrates significant generalization gains, achieving an average of 2.53 dB PSNR improvement over the strong baseline AdaIR.

Method	Dehazing		Deraining		Denoising		Deblurring		Low-Light		Average	
	PSNR	SSIM	PSNR	SSIM	PSNR	SSIM	PSNR	SSIM	PSNR	SSIM	PSNR	SSIM
AirNet	16.13	0.465	18.93	0.657	25.78	0.841	-	-	-	-	20.28	0.654
PromptIR	16.45	0.472	19.47	0.686	30.99	0.918	-	-	-	-	22.30	0.692
AdaIR	16.71	0.475	19.58	0.684	28.83	0.902	20.43	0.806	15.96	0.781	20.30	0.730
IRPO	19.94	0.623	21.17	0.692	33.18	0.919	21.94	0.837	22.43	0.875	23.73	0.809

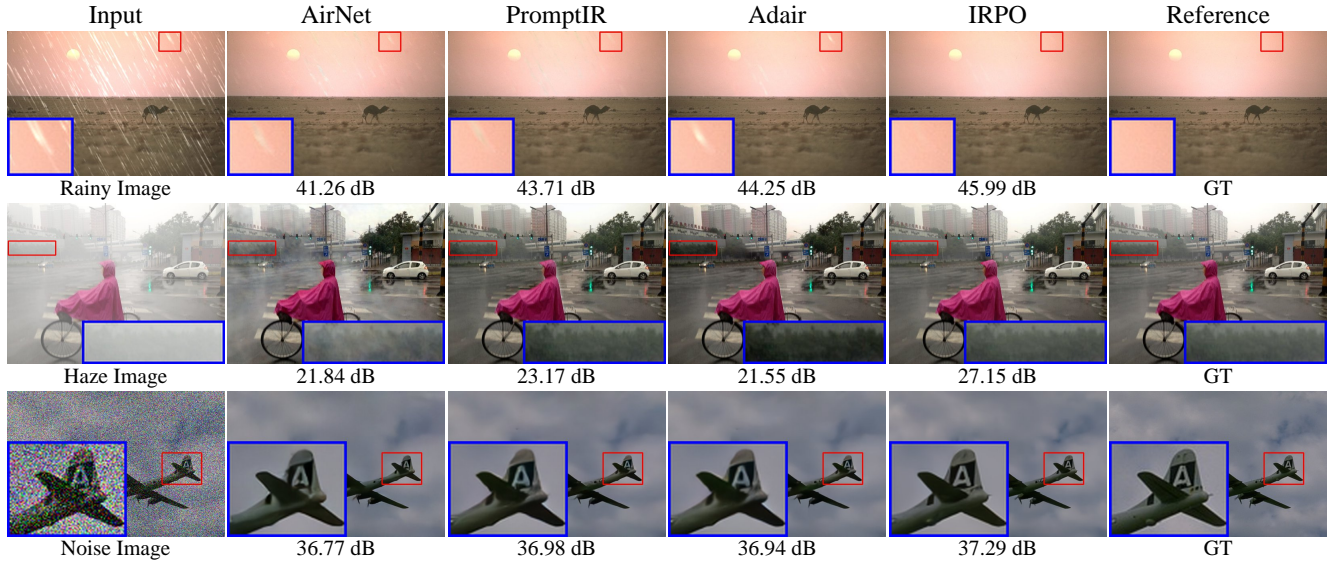


Figure 3. Visual comparisons for different restoration tasks. The first row is derain, the second row is dehaze, and the third row is denoise (noise level 50). Please zoom in for better details.

challenging OOD datasets corresponding to our five tasks (results shown in Table 3). For dehazing, we use RRSID [83], a real-world paired dataset specifically designed for residual-streak-based image dehazing. For deraining, we use GT-Rain [3], a high-quality real-world dataset that provides ground-truth rain-free images by capturing scenes before and after rain events, moving beyond simple streak simulation. For real-world denoising, we use the Smartphone Image Denoising Dataset (SIDD) [1], a widely-used benchmark containing real-world noise captured from various smartphone cameras. For real-world deblurring, we use the ReLoBlur dataset [34], which focuses on real-world deep local motion deblurring by providing high-resolution video frames with complex local motion. Finally, for OOD low-light enhancement, we use the LoLi-Street dataset [23], which features challenging real-world street scenes with paired low-light and long-exposure ground-truth images.

Implementation Details. Our IRPO framework is initialized with the pre-trained AdaIR [10] backbone, preserving its 4-level encoder-decoder structure with [4, 6, 6, 8]

transformer blocks and three AFLB modules. We introduce lightweight policy heads to each AFLB to parameterize the 4-dimensional Beta distributions for actions (r_h, r_l, g_f, g_o) . Crucially, we identify and fine-tune only on the 30% of training samples with the lowest initial restoration quality. During GRPO fine-tuning, we set the group size $G = 4$ and 30 epochs total.

Optimization is performed using Adam ($\beta_1 = 0.9, \beta_2 = 0.999$) with a base learning rate of 3×10^{-5} for 30 epochs. To stabilize RL training, we apply higher learning rate multipliers to the policy heads ($6\times$). We further incorporate auxiliary objectives with linear annealing schedules: a supervised \mathcal{L}_1 loss on the best candidate (λ_{sup} : start from 0.35 to 0.1 end) and a consistency constraint (λ_{cons} : start from 0.2 to 0.05 end). Following AdaIR [10], we use 128×128 random crops and standard augmentations. The model is trained on two NVIDIA 4090 GPUs with a batch size of one per GPU and additional two GPUs to deploy Qwen2.5-VL-7B-Instruct model. A comprehensive list of hyperparameters is provided in Appendix C.

Table 4. Ablation study on the reward components. We compare the Baseline (AdaIR) with models post-trained by adding each of our three reward components (R_{gen} , R_{qwen} , R_{task}) individually.

Method	Dehazing	Deraining	Denoising	Deblurring	Low-Light	Average
Baseline	30.53/0.978	38.02/0.981	31.35/0.889	28.12/0.858	23.0/0.845	30.2/0.910
+ R_{gen}	31.08/0.980	38.57/0.985	31.95/0.893	28.64/0.861	23.68/0.852	30.78/0.914
+ R_{qwen}	30.71/0.979	38.28/0.983	31.64/0.891	28.35/0.859	23.31/0.848	30.46/0.912
+ R_{task}	30.89/0.980	38.42/0.984	31.83/0.893	28.57/0.861	23.57/0.850	30.66/0.914
IRPO	31.36/0.982	38.72/0.987	32.13/0.896	28.89/0.863	24.08/0.858	31.04/0.917

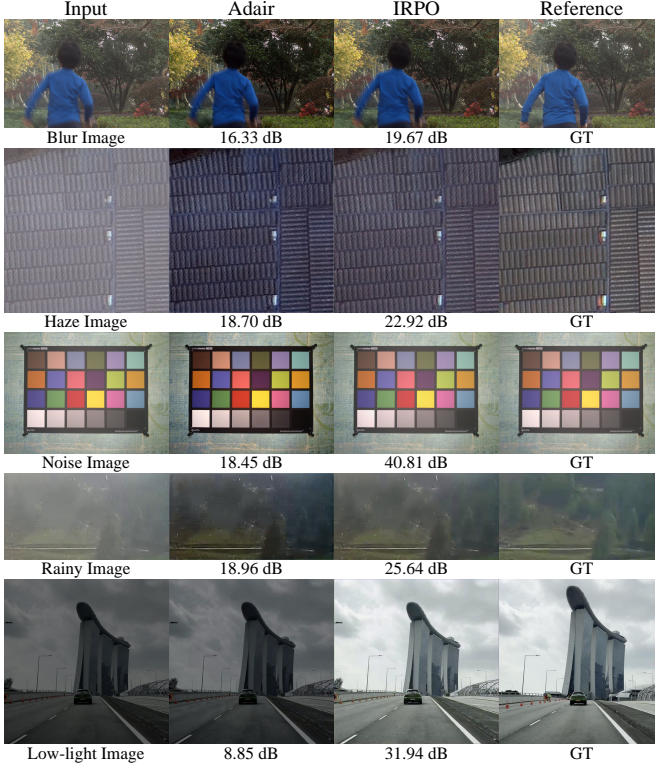


Figure 4. Visual comparisons on real-world datasets. From top to bottom: deblurring, dehazing, denoising, deraining, and low-light enhancement. Please zoom in for better details.

Table 5. Ablation study on the GRPO group size (G). Performance is measured by average PSNR (dB) on the all-in-one 5-task benchmark. $G = 4$ provides the optimal trade-off between performance and computational cost.

Group	Dehazing	Deraining	Denoising	Deblurring	Low-Light	Average
3	31.27	38.59	31.89	28.32	24.03	30.82
4	31.36	38.72	32.13	28.89	24.08	31.04
5	31.35	38.71	32.15	28.91	24.05	31.03

4.2. Main Experiments

We validate the efficacy of our proposed IRPO framework through comprehensive experiments on both standard single-task benchmarks and more challenging all-in-one settings.

Single-Task Restoration. We first evaluate IRPO by training separate, specialized models for three core low-level tasks. As shown in Table 1, our GRPO post-training strategy demonstrates a clear and consistent advantage across the board. On all three tasks (dehazing, deraining, and denoising), IRPO achieves new state-of-the-art (SOTA) performance, surpassing all competitors including the strong AdaIR baseline and PromptIR. For instance, IRPO outperforms PromptIR by a significant 1.0 dB on dehazing (Table 1a) and 2.34 dB on deraining (Table 1b). Notably, on the challenging Urban100 ($\sigma = 50$) denoising task (Table 1c), our method achieves the largest gain of +0.37 dB, highlighting its robustness to heavy degradations.

All-in-One Restoration. We now focus on the more complex all-in-one setting, which serves as an extension of the basic low-level tasks. We compare IRPO against (1) general-purpose IR methods (*e.g.*, NAFNet, Restormer) and (2) specialized all-in-one approaches (*e.g.*, PromptIR, AdaIR). As shown in Table 2 (five-degradation setting), our IRPO again achieves SOTA performance across all five tasks. The results clearly indicate that our GRPO post-training successfully elevates the performance ceiling of the already-strong AdaIR baseline. Compared to AdaIR, IRPO achieves consistent performance gains across all metrics, culminating in a significant 0.83 dB average PSNR improvement. The boost is particularly significant on low-light enhancement (+1.08 dB) and denoising (+0.78 dB). We also provide visual examples in Figure 3 for dehazing, deraining, and denoising. These examples show that our IRPO is effective in removing degradations, and generates images that are visually closer to the ground truth than AdaIR. More result in image restoration can be seen in Appendix E and visual result can be seen in Appendix F.

4.3. Evaluation on Out-of-Domain (OOD) Generalization

One of the central challenges for all-in-one models is their generalization capability. To assess the performance of IRPO on unseen OOD data, we evaluate it on a comprehensive OOD test set (Table 3). This dataset, comprising degradation types and levels unseen during training, serves as a crucial litmus test for the model’s generalization.

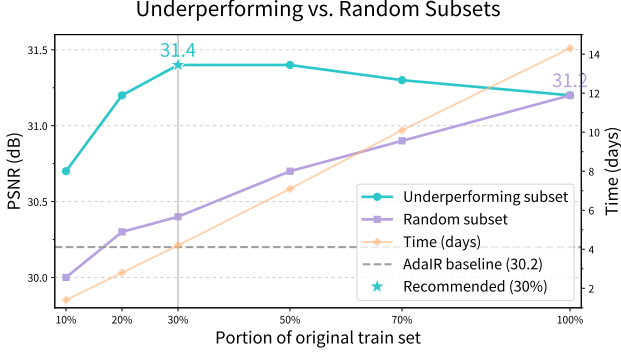


Figure 5. Post-training on underperforming vs. random subsets for the All-in-One five tasks. The left y-axis shows average PSNR (dB) and the right y-axis shows post-training time (GPU days); the dashed line marks the AdaIR baseline (30.2 dB). Balancing accuracy and cost, the 30% underperforming subset offers the best trade-off (31.4 dB in 4.2 days, comparable to 100% data but three times faster).

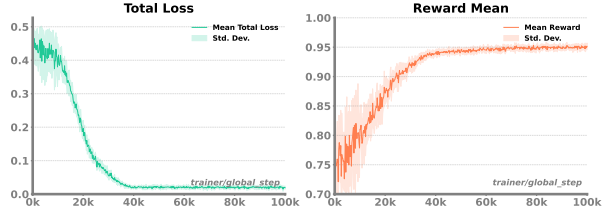


Figure 6. Training curves for our IRPO post-training (*mean* and *std. dev.* over 30 epoch). (Left) The Total Loss ($\mathcal{L}_{\text{total}}$) smoothly converges, demonstrating training stability. (Right) The reward mean steadily increases and converges to a high plateau, proving the policy is effectively learning to optimize our reward objectives.

Our method achieves an average PSNR of 23.73 dB, which is a significant 3.43 dB improvement over the baseline AdaIR’s 20.30 dB. Similarly, the average SSIM is boosted from 0.730 to 0.809. This result strongly supports our motivation: conventional L1/L2 losses tend to overfit to the training distribution, leading to limited generalization (as seen by AdaIR’s modest OOD performance). In contrast, our IRPO successfully breaks free from the constraints of pixel-level loss. The model is no longer memorizing the training data but is learning a more generalizable restoration policy that aligns better with human preference and real-world priors. The radical improvements, especially on low-light +6.47 dB and denoising +4.35 dB, establish our framework as a new and effective paradigm for enhancing the generalization of low-level vision models. We provide visual examples in Figure 4 for dehazing, deraining, denoising, deblurring, and low-light enhancement. Adair struggles to correctly identify the specific degradation type in OOD degraded images, leading to incorrect restoration like the low-light image, while IRPO exhibits significantly better generalization performance on OOD data.

4.4. Ablation Study

We conduct comprehensive ablation studies to validate the core components of our proposed paradigm. We analyze the data selection strategy, the contribution of each reward, the GRPO group size, and overall training stability.

Effect of Data Portion. As shown in Figure 5, we validate our data-oriented approach. Fine-tuning on randomly sampled data (purple line) scales poorly with data size and computational cost. In contrast, focusing on the underperforming subset (teal line) provides a much stronger and more efficient performance gain. We identify 30% as the optimal trade-off, achieving 31.4 dB (a +1.2 dB gain over baseline) in 4.2 GPU days, which is 3× faster than model trained on 100% data.

Effect of Reward Components. We analyze the contribution of each reward component in Table 4. Fine-tuning the baseline (30.20 dB) with R_{gen} provides the largest individual boost (+0.58 dB), confirming the value of its aggregated perceptual metrics. While R_{task} (+0.46 dB) delivers a clear boost, the smaller gain from R_{qwen} (+0.26 dB) may stem from its lack of a concrete metric and the potential hallucinations from Qwen. Our full IRPO model (31.04 dB), which combines all three, outperforms any individual component, proving that the general, expert, and task-specific rewards are complementary and work in synergy.

Effect of GRPO Group Size. We investigate the impact of the GRPO group size G in Table 5. We observe that $G = 3$ (30.82 dB) is suboptimal, likely due to unstable advantage estimates. Increasing G to 4 provides a significant performance jump to 31.04 dB. $G = 5$ (31.03 dB) yields no further meaningful benefits while increasing computational cost. Thus, we choose $G = 4$ as the optimal trade-off between performance and efficiency.

Training Stability. As visualized in Figure 6, the total loss (left) smoothly converges without divergence, while the mean reward (right) consistently increases and saturates at a high value. This demonstrates that our policy effectively learns to optimize the complex reward signals without sacrificing training stability.

5. Conclusion

This study introduces IRPO, the first low-level post-training paradigm centered on GRPO, which systematically enhances model robustness and perceptual quality. Our work makes two key contributions to this new paradigm. First, we explore and validate a data-oriented principle, demonstrating that focusing post-training on the 30% underperforming hard data is the most effective and efficient strategy. Second, we design a reward-oriented framework with three complementary components (General, Expert, and Task-Aware) to align the model with human preferences and task-specific quality standards. Extensive experiments show that

our paradigm achieves SOTA performance with strong generalization on OOD benchmarks. We hope the principles of data-centric and reward-centric optimization presented in IRPO will encourage further research into more robust and human-aligned image restoration.

References

- [1] Abdelrahman Abdelhamed, Stephen Lin, and Michael S Brown. A high-quality denoising dataset for smartphone cameras. In *Proceedings of the IEEE conference on computer vision and pattern recognition*, pages 1692–1700, 2018. 6
- [2] Pablo Arbelaez, Michael Maire, Charless Fowlkes, and Jitendra Malik. Contour detection and hierarchical image segmentation. *TPAMI*, 2010. 5
- [3] Yunhao Ba, Howard Zhang, Ethan Yang, Akira Suzuki, Arnold Pfahnl, Chethan Chinder Chandrappa, Celso M De Melo, Suyu You, Stefano Soatto, Alex Wong, et al. Not just streaks: Towards ground truth for single image deraining. In *European Conference on Computer Vision*, pages 723–740. Springer, 2022. 6
- [4] Yuntao Bai, Andy Jones, Kamal Ndousse, Amanda Askell, Anna Chen, Nova DasSarma, Dawn Drain, Stanislav Fort, Deep Ganguli, Tom Henighan, et al. Training a helpful and harmless assistant with reinforcement learning from human feedback. *arXiv preprint arXiv:2204.05862*, 2022. 3
- [5] Yochai Blau and Tomer Michaeli. The perception-distortion tradeoff. In *Proceedings of the IEEE conference on computer vision and pattern recognition*, pages 6228–6237, 2018. 2, 3
- [6] Bolun Cai, Xiangmin Xu, Kui Jia, Chunmei Qing, and Dacheng Tao. Dehazenet: An end-to-end system for single image haze removal. *TIP*, 2016. 5
- [7] Liangyu Chen, Xin Lu, Jie Zhang, Xiaojie Chu, and Chengpeng Chen. Hinet: Half instance normalization network for image restoration. In *CVPR Workshops*, 2021. 5
- [8] Liangyu Chen, Xiaojie Chu, Xiangyu Zhang, and Jian Sun. Simple baselines for image restoration. In *ECCV*, 2022. 5
- [9] Liang Chen, Lei Li, Haozhe Zhao, and Yifan Song. Vinci. r1-v: Reinforcing super generalization ability in vision-language models with less than \$3, 2025. 3
- [10] Yuning Cui, Syed Waqas Zamir, Salman Khan, Alois Knoll, Mubarak Shah, and Fahad Shahbaz Khan. AdaIR: Adaptive all-in-one image restoration via frequency mining and modulation. In *The Thirteenth International Conference on Learning Representations*, 2025. 2, 4, 5, 6, 3
- [11] Kostadin Dabov, Alessandro Foi, Vladimir Katkovnik, and Karen Egiazarian. Color image denoising via sparse 3d collaborative filtering with grouping constraint in luminance-chrominance space. In *ICIP*, 2007. 5
- [12] Chao Dong, Chen Change Loy, Kaiming He, and Xiaoou Tang. Image super-resolution using deep convolutional networks. *IEEE transactions on pattern analysis and machine intelligence*, 38(2):295–307, 2015. 2
- [13] Yu Dong, Yihao Liu, He Zhang, Shifeng Chen, and Yu Qiao. Fd-gan: Generative adversarial networks with fusion-discriminator for single image dehazing. In *AAAI*, 2020. 5, 4
- [14] Qingnan Fan, Dongdong Chen, Lu Yuan, Gang Hua, Nenghai Yu, and Baoquan Chen. A general decoupled learning framework for parameterized image operators. *TPAMI*, 2019. 5, 4
- [15] Hongyun Gao, Xin Tao, Xiaoyong Shen, and Jiaya Jia. Dynamic scene deblurring with parameter selective sharing and nested skip connections. In *CVPR*, 2019. 5, 4
- [16] Xinyan Guan, Yanjiang Liu, Xinyu Lu, Boxi Cao, Ben He, Xianpei Han, Le Sun, Jie Lou, Bowen Yu, Yaojie Lu, et al. Search, verify and feedback: Towards next generation post-training paradigm of foundation models via verifier engineering. *arXiv preprint arXiv:2411.11504*, 2024. 1
- [17] Daya Guo, Dejian Yang, Haowei Zhang, Junxiao Song, Ruoyu Zhang, Runxin Xu, Qihao Zhu, Shirong Ma, Peiyi Wang, Xiao Bi, et al. Deepseek-r1: Incentivizing reasoning capability in llms via reinforcement learning. *arXiv preprint arXiv:2501.12948*, 2025. 3
- [18] Shi Guo, Zifei Yan, Kai Zhang, Wangmeng Zuo, and Lei Zhang. Toward convolutional blind denoising of real photographs. In *Proceedings of the IEEE/CVF conference on computer vision and pattern recognition*, pages 1712–1722, 2019. 3
- [19] Xiaobin Hu, Wenqi Ren, John LaMaster, Xiaochun Cao, Xiaoming Li, Zechao Li, Bjoern Menze, and Wei Liu. Face super-resolution guided by 3d facial priors. In *European Conference on Computer Vision*, pages 763–780. Springer, 2020. 3
- [20] Xiaobin Hu, Wenqi Ren, Jiaolong Yang, Xiaochun Cao, David Wipf, Bjoern Menze, Xin Tong, and Hongbin Zha. Face restoration via plug-and-play 3d facial priors. *IEEE Transactions on Pattern Analysis and Machine Intelligence*, 44(12):8910–8926, 2021. 3
- [21] Jia-Bin Huang, Abhishek Singh, and Narendra Ahuja. Single image super-resolution from transformed self-exemplars. In *CVPR*, 2015. 5
- [22] Team Hunyuan3D, Bowen Zhang, Chunchao Guo, Haolin Liu, Hongyu Yan, Huiwen Shi, Jingwei Huang, Junlin Yu, Kunhong Li, Penghao Wang, et al. Hunyuan3d-omni: A unified framework for controllable generation of 3d assets. *arXiv preprint arXiv:2509.21245*, 2025. 1
- [23] Md Tanvir Islam, Inzamamul Alam, Simon S Woo, Saeed Anwar, IK Lee, and Khan Muhammad. Loli-street: Benchmarking low-light image enhancement and beyond. In *Proceedings of the Asian Conference on Computer Vision*, pages 1250–1267, 2024. 6
- [24] Aaron Jaech, Adam Kalai, Adam Lerer, Adam Richardson, Ahmed El-Kishky, Aiden Low, Alec Helyar, Aleksander Madry, Alex Beutel, Alex Carney, et al. Openai o1 system card. *arXiv preprint arXiv:2412.16720*, 2024. 3
- [25] Viren Jain, Joseph F Murray, Fabian Roth, Srinivas Turaga, Valentin Zhigulin, Kevin L Briggman, Moritz N Helms, Winfried Denk, and H Sebastian Seung. Supervised learning of image restoration with convolutional networks. In *2007 IEEE 11th International Conference on Computer Vision*, pages 1–8. IEEE, 2007. 2
- [26] Xiaozhong Ji, Xiaobin Hu, Zhihong Xu, Junwei Zhu, Chuming Lin, Qingdong He, Jiangning Zhang, Donghao Luo, Yi

- Chen, Qin Lin, et al. Sonic: Shifting focus to global audio perception in portrait animation. In *Proceedings of the Computer Vision and Pattern Recognition Conference*, pages 193–203, 2025. 1
- [27] Kui Jiang, Zhongyuan Wang, Peng Yi, Chen Chen, Baojin Huang, Yimin Luo, Jiayi Ma, and Junjun Jiang. Multi-scale progressive fusion network for single image deraining. In *CVPR*, 2020. 5
- [28] Justin Johnson, Alexandre Alahi, and Li Fei-Fei. Perceptual losses for real-time style transfer and super-resolution. In *European conference on computer vision*, pages 694–711. Springer, 2016. 2, 3
- [29] Xiaoqiang Kang, Shengen Wu, Zimu Wang, Yilin Liu, Xiaobo Jin, Kaizhu Huang, Wei Wang, Yutao Yue, Xiaowei Huang, and Qiufeng Wang. Can grpo boost complex multimodal table understanding? In *Proceedings of the 2025 Conference on Empirical Methods in Natural Language Processing*, pages 12642–12655, 2025. 3
- [30] Hanyu Lai, Xiao Liu, Junjie Gao, Jiale Cheng, Zehan Qi, Yifan Xu, Shuntian Yao, Dan Zhang, Jinhua Du, Zhenyu Hou, et al. A survey of post-training scaling in large language models. In *Proceedings of the 63rd Annual Meeting of the Association for Computational Linguistics (Volume 1: Long Papers)*, pages 2771–2791, 2025. 1
- [31] Jaakko Lehtinen, Jacob Munkberg, Jon Hasselgren, Samuli Laine, Tero Karras, Miika Aittala, and Timo Aila. Noise2noise: Learning image restoration without clean data. *arXiv preprint arXiv:1803.04189*, 2018. 2, 3
- [32] Boyi Li, Wenqi Ren, Dengpan Fu, Dacheng Tao, Dan Feng, Wenjun Zeng, and Zhangyang Wang. Benchmarking single-image dehazing and beyond. *TIP*, 2018. 5, 4
- [33] Boyun Li, Xiao Liu, Peng Hu, Zhongqin Wu, Jiancheng Lv, and Xi Peng. All-in-one image restoration for unknown corruption. In *CVPR*, 2022. 3, 5, 4
- [34] Haoying Li, Ziran Zhang, Tingting Jiang, Peng Luo, Huajun Feng, and Zhihai Xu. Real-world deep local motion deblurring. In *proceedings of the AAAI conference on artificial intelligence*, pages 1314–1322, 2023. 6
- [35] Jiachen Li, Qian Long, Jian Zheng, Xiaofeng Gao, Robinson Piramuthu, Wenhui Chen, and William Yang Wang. T2v-turbo-v2: Enhancing video generation model post-training through data, reward, and conditional guidance design. *arXiv preprint arXiv:2410.05677*, 2024. 1, 3
- [36] Jingyun Liang, Jiezhong Cao, Guolei Sun, Kai Zhang, Luc Van Gool, and Radu Timofte. Swinir: Image restoration using swin transformer. In *Proceedings of the IEEE/CVF international conference on computer vision*, pages 1833–1844, 2021. 2, 5
- [37] Jingyun Liang, Jiezhong Cao, Yuchen Fan, Kai Zhang, Rakesh Ranjan, Yawei Li, Radu Timofte, and Luc Van Gool. Vrt: A video restoration transformer. *IEEE Transactions on Image Processing*, 33:2171–2182, 2024. 3
- [38] Yujie Liang, Xiaobin Hu, Boyuan Jiang, Donghao Luo, Xu Peng, Kai Wu, Chengming Xu, Wenhui Han, Taisong Jin, Chengjie Wang, et al. Vton-handfit: Virtual try-on for arbitrary hand pose guided by hand priors embedding. In *Proceedings of the Computer Vision and Pattern Recognition Conference*, pages 22616–22626, 2025. 1
- [39] Shanchuan Lin, Xin Xia, Yuxi Ren, Ceyuan Yang, Xuefeng Xiao, and Lu Jiang. Diffusion adversarial post-training for one-step video generation. *arXiv preprint arXiv:2501.08316*, 2025. 1
- [40] Shanchuan Lin, Ceyuan Yang, Hao He, Jianwen Jiang, Yuxi Ren, Xin Xia, Yang Zhao, Xuefeng Xiao, and Lu Jiang. Autoregressive adversarial post-training for real-time interactive video generation. *arXiv preprint arXiv:2506.09350*, 2025. 1
- [41] Lin Liu, Lingxi Xie, Xiaopeng Zhang, Shanxin Yuan, Xianguyu Chen, Wengang Zhou, Houqiang Li, and Qi Tian. Tape: Task-agnostic prior embedding for image restoration. In *ECCV*, 2022. 5
- [42] Lu Liu, Chunlei Cai, Shaocheng Shen, Jianfeng Liang, Weimin Ouyang, Tianxiao Ye, Jian Mao, Huiyu Duan, Jiangchao Yao, Xiaoyun Zhang, et al. Moa-vr: A mixture-of-agents system towards all-in-one video restoration. *arXiv preprint arXiv:2510.08508*, 2025. 2, 3
- [43] Lei Liu, Luan Ma, Shuai Wang, Jun Wang, and Silas N Melo. Two-stage mamba-based diffusion model for image restoration. *Scientific Reports*, 15(1):22265, 2025. 2
- [44] Zhenhua Liu, Yunhe Wang, Kai Han, Wei Zhang, Siwei Ma, and Wen Gao. Post-training quantization for vision transformer. *Advances in Neural Information Processing Systems*, 34:28092–28103, 2021. 1, 3
- [45] Kede Ma, Zhengfang Duanmu, Qingbo Wu, Zhou Wang, Hongwei Yong, Hongliang Li, and Lei Zhang. Waterloo exploration database: New challenges for image quality assessment models. *TIP*, 2016. 5
- [46] David Martin, Charles Fowlkes, Doron Tal, and Jitendra Malik. A database of human segmented natural images and its application to evaluating segmentation algorithms and measuring ecological statistics. In *ICCV*, 2001. 5, 4
- [47] Chong Mou, Qian Wang, and Jian Zhang. Deep generalized unfolding networks for image restoration. In *CVPR*, 2022. 5
- [48] Seungjun Nah, Tae Hyun Kim, and Kyoung Mu Lee. Deep multi-scale convolutional neural network for dynamic scene deblurring. In *CVPR*, 2017. 5
- [49] Vaishnav Potlapalli, Syed Waqas Zamir, Salman H Khan, and Fahad Shahbaz Khan. Promptir: Prompting for all-in-one image restoration. *NeurIPS*, 2023. 2, 5, 3, 4
- [50] Zhangyang Qi, Zhixiong Zhang, Yizhou Yu, Jiaqi Wang, and Hengshuang Zhao. Vln-r1: Vision-language navigation via reinforcement fine-tuning. *arXiv preprint arXiv:2506.17221*, 2025. 3
- [51] Yanyun Qu, Yizi Chen, Jingying Huang, and Yuan Xie. Enhanced pix2pix dehazing network. In *CVPR*, 2019. 5
- [52] Alec Radford, Jong Wook Kim, Chris Hallacy, Aditya Ramesh, Gabriel Goh, Sandhini Agarwal, Girish Sastry, Amanda Askell, Pamela Mishkin, Jack Clark, et al. Learning transferable visual models from natural language supervision. In *International conference on machine learning*, pages 8748–8763. PmLR, 2021. 1
- [53] Rafael Rafailov, Archit Sharma, Eric Mitchell, Christopher D Manning, Stefano Ermon, and Chelsea Finn. Direct preference optimization: Your language model is secretly a reward model. *Advances in neural information processing systems*, 36:53728–53741, 2023. 3

- [54] Wenqi Ren, Si Liu, Hua Zhang, Jinshan Pan, Xiaochun Cao, and Ming-Hsuan Yang. Single image dehazing via multi-scale convolutional neural networks. In *ECCV*, 2016. 5
- [55] Christoph Schuhmann, Romain Beaumont, Richard Vencu, Cade Gordon, Ross Wightman, Mehdi Cherti, Theo Coombes, Aarush Katta, Clayton Mullis, Mitchell Wortsman, et al. Laion-5b: An open large-scale dataset for training next generation image-text models. *Advances in neural information processing systems*, 35:25278–25294, 2022. 1
- [56] Yuzhang Shang, Zhihang Yuan, Bin Xie, Bingzhe Wu, and Yan Yan. Post-training quantization on diffusion models. In *Proceedings of the IEEE/CVF conference on computer vision and pattern recognition*, pages 1972–1981, 2023. 1
- [57] Zhihong Shao, Peiyi Wang, Qihao Zhu, Runxin Xu, Junxiao Song, Xiao Bi, Haowei Zhang, Mingchuan Zhang, YK Li, Yang Wu, et al. Deepseekmath: Pushing the limits of mathematical reasoning in open language models. *arXiv preprint arXiv:2402.03300*, 2024. 2, 3
- [58] Xiangfei Sheng, Xiaofeng Pan, Zhichao Yang, Pengfei Chen, and Leida Li. Fine-grained image quality assessment for perceptual image restoration. *arXiv preprint arXiv:2508.14475*, 2025. 1, 3
- [59] Chunwei Tian, Yong Xu, and Wangmeng Zuo. Image denoising using deep cnn with batch renormalization. *Neural Networks*, 2020. 5, 4
- [60] Hugo Touvron, Thibaut Lavril, Gautier Izacard, Xavier Martinet, Marie-Anne Lachaux, Timothée Lacroix, Baptiste Rozière, Naman Goyal, Eric Hambro, Faisal Azhar, et al. Llama: Open and efficient foundation language models. *arXiv preprint arXiv:2302.13971*, 2023. 3
- [61] Jeya Maria Jose Valanarasu, Rajeev Yasarla, and Vishal M Patel. Transweather: Transformer-based restoration of images degraded by adverse weather conditions. In *CVPR*, 2022. 5
- [62] Boyang Wang, Fengyu Yang, Xihang Yu, Chao Zhang, and Hanbin Zhao. Apisr: Anime production inspired real-world anime super-resolution. In *Proceedings of the IEEE/CVF Conference on Computer Vision and Pattern Recognition*, pages 25574–25584, 2024. 2
- [63] Xintao Wang, Ke Yu, Shixiang Wu, Jinjin Gu, Yihao Liu, Chao Dong, Yu Qiao, and Chen Change Loy. Esrgan: Enhanced super-resolution generative adversarial networks. In *Proceedings of the European conference on computer vision (ECCV) workshops*, pages 0–0, 2018. 3
- [64] Chen Wei, Wenjing Wang, Wenhan Yang, and Jiaying Liu. Deep retinex decomposition for low-light enhancement. *arXiv preprint arXiv:1808.04560*, 2018. 5
- [65] Gang Wu, Junjun Jiang, Kui Jiang, and Xianming Liu. Boosting all-in-one image restoration via self-improved privilege learning. *arXiv preprint arXiv:2505.24207*, 2025. 2
- [66] Haoxuan Xu, Songning Lai, Xianyang Li, and Yang Yang. Cross-domain car detection model with integrated convolutional block attention mechanism. *Image and Vision Computing*, 140:104834, 2023. 2
- [67] Wenhan Yang, Robby T Tan, Jiashi Feng, Zongming Guo, Shuicheng Yan, and Jiaying Liu. Joint rain detection and removal from a single image with contextualized deep networks. *TPAMI*, 2019. 5, 4
- [68] Yi Yang, Xiaoxuan He, Hongkun Pan, Xiyan Jiang, Yan Deng, Xingtao Yang, Haoyu Lu, Dacheng Yin, Fengyun Rao, Minfeng Zhu, et al. R1-onevision: Advancing generalized multimodal reasoning through cross-modal formalization. *arXiv preprint arXiv:2503.10615*, 2025. 2, 3
- [69] Rajeev Yasarla and Vishal M Patel. Uncertainty guided multi-scale residual learning-using a cycle spinning cnn for single image de-raining. In *CVPR*, 2019. 5
- [70] Angen Ye, Zeyu Zhang, Boyuan Wang, Xiaofeng Wang, Dapeng Zhang, and Zheng Zhu. V1a-r1: Enhancing reasoning in vision-language-action models. *arXiv preprint arXiv:2510.01623*, 2025. 3
- [71] Bo Yin, Xiaobin Hu, Xingyu Zhou, Peng-Tao Jiang, Yue Liao, Junwei Zhu, Jiangning Zhang, Ying Tai, Chengjie Wang, and Shuicheng Yan. Fera: Frequency-energy constrained routing for effective diffusion adaptation fine-tuning. *arXiv preprint arXiv:2511.17979*, 2025. 3
- [72] Syed Waqas Zamir, Aditya Arora, Salman Khan, Munawar Hayat, Fahad Shahbaz Khan, Ming-Hsuan Yang, and Ling Shao. Multi-stage progressive image restoration. In *Proceedings of the IEEE/CVF conference on computer vision and pattern recognition*, pages 14821–14831, 2021. 2, 5, 4
- [73] Syed Waqas Zamir, Aditya Arora, Salman Khan, Munawar Hayat, Fahad Shahbaz Khan, and Ming-Hsuan Yang. Restormer: Efficient transformer for high-resolution image restoration. In *CVPR*, 2022. 2, 5
- [74] Syed Waqas Zamir, Aditya Arora, Salman Khan, Munawar Hayat, Fahad Shahbaz Khan, Ming-Hsuan Yang, and Ling Shao. Learning enriched features for fast image restoration and enhancement. *TPAMI*, 2022. 2, 5
- [75] He Zhang and Vishal M Patel. Density-aware single image de-raining using a multi-stream dense network. In *CVPR*, 2018. 5
- [76] Jinghao Zhang, Jie Huang, Mingde Yao, Zizheng Yang, Hu Yu, Man Zhou, and Feng Zhao. Ingredient-oriented multi-degradation learning for image restoration. In *CVPR*, 2023. 5
- [77] Jingyi Zhang, Jiaxing Huang, Huanjin Yao, Shunyu Liu, Xikun Zhang, Shijian Lu, and Dacheng Tao. R1-vl: Learning to reason with multimodal large language models via step-wise group relative policy optimization. *arXiv preprint arXiv:2503.12937*, 2025. 3
- [78] Kai Zhang, Wangmeng Zuo, Yunjin Chen, Deyu Meng, and Lei Zhang. Beyond a gaussian denoiser: Residual learning of deep cnn for image denoising. *TIP*, 2017. 2, 3, 5
- [79] Kai Zhang, Wangmeng Zuo, Shuhang Gu, and Lei Zhang. Learning deep CNN denoiser prior for image restoration. In *CVPR*, 2017. 5
- [80] Kai Zhang, Wangmeng Zuo, and Lei Zhang. Ffdnet: Toward a fast and flexible solution for cnn-based image denoising. *TIP*, 2018. 5
- [81] Richard Zhang, Phillip Isola, Alexei A Efros, Eli Shechtman, and Oliver Wang. The unreasonable effectiveness of deep features as a perceptual metric. In *Proceedings of the IEEE conference on computer vision and pattern recognition*, pages 586–595, 2018. 1
- [82] Xiaoyu Zhang, Wei Gao, Ge Li, Qiuping Jiang, and Runmin Cong. Image quality assessment-driven reinforcement

- learning for mixed distorted image restoration. *ACM Transactions on Multimedia Computing, Communications and Applications*, 19(1s):1–23, 2023. [1](#)
- [83] Zeng-Hui Zhu, Wei Lu, Si-Bao Chen, Chris HQ Ding, Jin Tang, and Bin Luo. Real-world remote sensing image dehazing: Benchmark and baseline. *IEEE Transactions on Geoscience and Remote Sensing*, 2025. [6](#)
- [84] Liu Zhuang, Lin Wayne, Shi Ya, and Zhao Jun. A robustly optimized bert pre-training approach with post-training. In *Proceedings of the 20th chinese national conference on computational linguistics*, pages 1218–1227, 2021. [1](#)



IRPO: Boosting Image Restoration via Post-training GRPO

Supplementary Material

A. Background on GRPO

Our reward-oriented optimization pillar is based on Group Relative Policy Optimization (GRPO). Here, we provide the detailed formulation for completeness.

Given a context x (the degraded image), a behavior policy $\pi_{\theta_{\text{old}}}(\cdot | x)$ draws a group of G responses $\{a_i\}_{i=1}^G$ (actions, i.e., control parameters). Each corresponding output y_i is scored by our reward model R (Sec. 3.3) to produce $\{r_i\}_{i=1}^G$.

GRPO constructs a *group-normalized* relative advantage A_i within the same input group, which serves as a stable, value-free advantage estimate:

$$\bar{r} = \frac{1}{G} \sum_{i=1}^G r_i, \quad s = \sqrt{\frac{1}{G} \sum_{i=1}^G (r_i - \bar{r})^2 + \varepsilon},$$

$$A_i = \frac{r_i - \bar{r}}{s}. \quad (8)$$

Let the likelihood ratio be:

$$\rho_i(\theta) = \frac{\pi_{\theta}(a_i | x)}{\pi_{\theta_{\text{old}}}(a_i | x)}. \quad (9)$$

GRPO then maximizes a clipped surrogate objective $\mathcal{J}_{\text{GRPO}}(\theta)$, which is identical to PPO but replaces the standard advantage with A_i . It further enforces a KL penalty on a reference policy π_{ref} :

$$\mathcal{J}_{\text{GRPO}}(\theta) = \mathbb{E}_{x \sim \mathcal{D}, \{a_i\} \sim \pi_{\theta_{\text{old}}}} \left[\frac{1}{G} \sum_{i=1}^G \min \left(\rho_i(\theta) A_i, \text{clip}(\rho_i(\theta), 1 - \epsilon, 1 + \epsilon) A_i \right) - \beta \widehat{\mathcal{D}}_{\text{KL}}(\pi_{\theta}(\cdot | x) \parallel \pi_{\text{ref}}(\cdot | x)) \right]. \quad (10)$$

The KL divergence term is estimated on the batch using samples from $\pi_{\theta_{\text{old}}}$:

$$\widehat{\mathcal{D}}_{\text{KL}}(\pi_{\theta} \parallel \pi_{\text{ref}}) = \frac{1}{G} \sum_{i=1}^G \rho_i(\theta) [\log \pi_{\theta}(a_i | x) - \log \pi_{\text{ref}}(a_i | x)]. \quad (11)$$

The full objective used in the main paper, \mathcal{L}_{RL} (Eq. 6), is the negative of Eq. (10) plus an entropy bonus. A_i is treated as a stop-gradient statistic in practice.

B. Reward Details

Notation and utilities. We work with linear RGB in $[0, 1]$. Let \hat{y} denote the ground-truth image and y the restored output. Let $\text{clip}_{[0,1]}(t) = \min(\max(t, 0), 1)$ and $\varepsilon = 10^{-6}$. For luminance we use $Y = 0.299R + 0.587G + 0.114B$. Sobel gradients of an

image Z are $G_x = \text{Sobel}_x(Z)$, $G_y = \text{Sobel}_y(Z)$, and magnitude $M(Z) = \sqrt{G_x^2 + G_y^2} + 10^{-12}$. When needed, $\mu(\cdot)$, $\sigma^2(\cdot)$, and $\text{std}(\cdot)$ denote spatial mean, variance, and standard deviation.

B.1. Generic Quality Term R_{gen}

This reward is a comprehensive blend of five metrics, each normalized to $[0, 1]$.

$$R_{\text{gen}}(y, \hat{y}) = 0.25 \cdot R_{\text{clip}}(y, \hat{y}) + 0.25 \cdot R_{\text{LPIPS}}(y, \hat{y}) + 0.15 \cdot R_{\text{aes}}(y) + 0.20 \cdot R_{\text{PSNR}}(y, \hat{y}) + 0.15 \cdot R_{\text{SSIM}}(y, \hat{y})$$

where R_{clip} is the CLIP similarity [52], R_{LPIPS} is the normalized LPIPS perceptual score [81], R_{aes} is a normalized aesthetic score from a pre-trained predictor [55], R_{PSNR} is the PSNR score mapped to $[0, 1]$ via fixed thresholds (τ_{\min}, τ_{\max}), and R_{SSIM} is the standard SSIM score.

B.2. Qwen-based Verifier R_{qwen}

We use Qwen-2.5VL-7B model as an expert judge. We provide it with the degraded input (x), the restored output (y), and the ground-truth (\hat{y}). The model provides a score from 1 to 5, which we linearly rescale.

B.3. Task-aware Shaping R_{task}

For each degradation type, we define a specialized reward.

(1) Denoising — gradient consistency. Let $M_g = M(Y_g)$, $M_{\text{rest}} = M(y)$. Define the GT baseline and mean magnitude deviation:

$$B = \mu(M_g), \quad D = \mu(|M_{\text{rest}} - M_g|). \quad (12)$$

The reward encourages the restored gradients to approach the clean target:

$$R_{\text{grad}} = \text{clip}_{[0,1]} \left(1 - \frac{D}{B + \varepsilon} \right). \quad (13)$$

This reward ensures that the restored image's texture and edge gradients (M_{rest}) statistically match the ground truth (M_g), preventing the common failure mode of over-smoothing (i.e., "losing" texture) during denoising.

(2) Deraining — anisotropy consistency. Compute average absolute Sobel responses on luminance:

$$E_x = \mu(|G_x(y)|), \quad E_y = \mu(|G_y(y)|). \quad (14)$$

Define normalized anisotropy

$$A = \frac{|E_x - E_y|}{\max(E_x + E_y, \varepsilon)}. \quad (15)$$

The reward favors isotropy (i.e., $A \approx 0$):

$$R_{\text{aniso}} = 1 - \text{clip}_{[0,1]}(A). \quad (16)$$

Qwen-VL Verifier Prompt

You are an image-restoration expert. You will be given three images:

1. The degraded input that suffers from a certain type of degradation.
2. The restored output generated by a model.
3. The clean ground-truth reference.

Task:

1. Identify the most plausible degradation type of the input image. Consider categories such as denoising (0/1/2, different noise levels), deraining (3), dehazing (4), deblurring (5), or low-light enhancement (6). Briefly justify your reasoning.
2. Compare the restored output against the ground truth with respect to the identified degradation type. Pay attention to:
 - Noise or streak removal quality for denoising/deraining.
 - Contrast and haze removal for dehazing.
 - Sharpness recovery for deblurring.
 - Exposure and color constancy for low-light enhancement.
3. Highlight specific improvements and any remaining artifacts.
4. Provide a final quality score from 1 to 5, where:
 - 1: severe artifacts or almost no improvement,
 - 2: minor improvement but significant issues remain,
 - 3: moderate improvement with noticeable gaps,
 - 4: strong restoration with only small flaws,
 - 5: near-perfect restoration indistinguishable from ground truth.

Respond in the following XML-style format:

```
<Assessment>
  <Degradation>
    [type and reasoning]
  </Degradation>
  <Analysis>
    [detailed comparison]
  </Analysis>
  <Score>X</Score>
</Assessment>
```

Rain streaks are highly anisotropic (directional), creating a strong bias in gradient orientation ($E_x \neq E_y$). A clean, rain-free image is typically isotropic ($E_x \approx E_y$). This reward pushes the model to produce an isotropic output, which is characteristic of a successfully derained image.

(3) Dehazing — contrast closeness. Let $C(Z) = \text{std}(Y_Z)$ be a proxy for the contrast of image Z . We measure symmetry-aware contrast closeness to ground truth:

$$R_{\text{contrast}} = \text{clip}_{[0,1]} \left(\min \left(\frac{C_{\text{rest}}}{C_g + \varepsilon}, \frac{C_g}{C_{\text{rest}} + \varepsilon} \right) \right). \quad (17)$$

Haze is a low-frequency component that severely reduces image contrast (lowers $\text{std}(Y)$). This reward ensures the restored image’s contrast C_{rest} is restored to the level of the ground truth C_g , penalizing both under-enhancement (remaining haze) and over-enhancement (oversaturation).

(4) Deblurring — sharpness closeness. Using the mean gradient magnitude $S(Z) = \mu(M(Z))$ as a proxy for sharpness:

$$R_{\text{sharp}} = \text{clip}_{[0,1]} \left(\min \left(\frac{S_{\text{rest}}}{S_g + \varepsilon}, \frac{S_g}{S_{\text{rest}} + \varepsilon} \right) \right). \quad (18)$$

Blurring is a loss of high-frequency information, resulting in low gradient magnitudes (low sharpness). This reward, similar to contrast, pushes the mean sharpness S_{rest} to match the ground truth S_g , directly encouraging the recovery of edges and details.

(5) Low-light — exposure & color consistency. Exposure alignment on luminance means:

$$d = |\mu(y) - \mu(Y_g)|, \quad R_{\text{exp}} = \text{clip}_{[0,1]} \left(1 - \frac{d}{0.5} \right). \quad (19)$$

Color consistency sums mean-channel deviations ($c \in \{R, G, B\}$):

$$d_c = \sum_c |\mu(c_{\text{rest}}) - \mu(c_g)|, \quad R_{\text{color}} = \text{clip}_{[0,1]} \left(1 - \frac{d_c}{0.6} \right). \quad (20)$$

Low-light enhancement has two goals: fidelity and brightness. R_{exp} ensures the overall luminance $\mu(y)$ matches the target, while R_{color} prevents color shifts (e.g., a green or purple tint) by penalizing deviation in individual R, G, B channels.

Putting the task terms together. For each sample, we select the reward(s) corresponding to its degradation:

$$\begin{aligned} R_{\text{task}}^{(\text{denoise})} &= R_{\text{grad}}, \quad R_{\text{task}}^{(\text{derain})} = R_{\text{aniso}}, \\ R_{\text{task}}^{(\text{dehaze})} &= R_{\text{contrast}}, \quad R_{\text{task}}^{(\text{deblur})} = R_{\text{sharp}}, \\ R_{\text{task}}^{(\text{low-light})} &= 0.2 \cdot R_{\text{exp}} + 0.1 \cdot R_{\text{color}}. \end{aligned} \quad (21)$$

B.4. Final Reward Combination

The final reward signal used in Eq. (3) of the main paper is the weighted sum of the three components:

$$\begin{aligned} R(y, y_g) &= 0.6 \cdot R_{\text{gen}}(y, \hat{y}) \\ &\quad + 0.1 \cdot R_{\text{qwen}}(y) \\ &\quad + 0.3 \cdot R_{\text{task}}^{(k)}(y, \hat{y}) \end{aligned} \quad (22)$$

where k is the known degradation type for the training sample.

C. Additional Implementation Details

We provide a comprehensive list of hyperparameters used in our IRPO post-training in Table 6. These parameters cover the core model architecture, data handling, optimization, and the specific settings for the GRPO training phase.

Table 6. Detailed hyperparameters for IRPO post-training.

Hyperparameter	Value / Description
Base Channel Width (model_dim)	48
Encoder-Decoder Levels	4 levels
Transformer Blocks	[4, 6, 6, 8]
Multi-head Attention Heads	[1, 2, 4, 8]
Refinement Blocks	4
FFN Expansion Factor	2.66
Frequency Policy (AFLB)	3 modules inserted between decoder levels
Action Space	4D continuous $(r_h, r_l, g_f, g_o) \in (0, 1)^4$
Input Patch Size	128×128
Augmentation	Random horizontal/vertical flips
Hard-Mining Ratio	Top 30% hardest samples
Optimizer	Adam ($\beta_1 = 0.9, \beta_2 = 0.999$)
Base Learning Rate (LR)	3×10^{-5}
Total Epochs	30 (default for main results)
Batch Size	1 per GPU (constrained by $G = 4$)
Group Size (G)	4
Entropy Regularization	0.01
Supervised Loss Weight (λ_{sup})	Linear decay: $0.35 \rightarrow 0.1$
Consistency Loss Weight (λ_{cons})	Linear decay: $0.2 \rightarrow 0.05$

D. Policy Parametrization Details

Our policy π_θ consists of 6 independent policy heads distributed across the 3 AFLB modules in the AdaIR decoder. Each AFLB module contains two heads: (1) a **Policy Rate** head, and (2) a **Policy Fuse** head, which correspond to the actions (r_h, r_l) and (g_f, g_o) respectively.

Policy Rate Head (r_h, r_l). The Policy Rate head determines the size of the frequency-domain mask.

- **Input:** It takes the initial degraded image x (which is fed to all AFLB modules) and passes it through an FFT.
- **Process:** A small CNN head takes the pooled features of x and outputs four positive scalars $(\alpha_h, \beta_h, \alpha_l, \beta_l)$.
- **Action:** These scalars parameterize two Beta distributions. During training, we sample $r_h \sim \text{Beta}(\alpha_h, \beta_h)$ and $r_l \sim \text{Beta}(\alpha_l, \beta_l)$. These actions $(r_h, r_l) \in (0, 1)^2$ define the height and width of the low-frequency mask. This mask is applied to the FFT of x to separate frequency components, which are then used to generate the intermediate feature O_i (the "Output Feature" in Figure 2).

Policy Fuse Head (g_f, g_o). The "Policy Fuse" head determines how to blend the intermediate feature with the decoder's latent feature.

- **Input:** It takes the latent feature y_i (the "Latent Feature" in Figure 2) coming from the previous decoder block.
- **Process:** A separate small CNN head takes the pooled features of y_i and outputs four positive scalars $(\alpha_1, \beta_1, \alpha_2, \beta_2)$.
- **Action:** We sample $g_l \sim \text{Beta}(\alpha_1, \beta_1)$ and $g_o \sim \text{Beta}(\alpha_2, \beta_2)$. These actions $(g_f, g_o) \in (0, 1)$ are the dynamic

weights used in the final fusion, as shown in Eq. (5) in the main paper.

Log-Probability Calculation. The policy π_θ is the joint distribution of these 4 independent actions. The log-probability $\log \pi_\theta(a|x, y)$ is required for the policy gradient calculation (e.g., in Eq. 11). This function has the following closed form:

$$\log \pi_\theta(a|x, y) = \sum_{k \in \{h, l, f, o\}} \left[(\alpha_k - 1) \log a_k + (\beta_k - 1) \log(1 - a_k) \right] - \sum_{k \in \{h, l, f, o\}} \log B(\alpha_k, \beta_k), \quad (23)$$

where a_k is the sampled action for $k \in \{h, l, f, o\}$, (α_k, β_k) are the distribution parameters output by the corresponding policy head, and $B(\cdot, \cdot)$ is the Beta function.

E. Additional Experiment Results

The superiority of our model is further validated in the three-degradation setting (Table 7). IRPO comprehensively outperforms all competitors, surpassing AdaIR by 0.69 dB and the strong SOTA method PromptIR by 1.32 dB. A key observation is the 1.37 dB gain on the heavy noise ($\sigma = 50$) test, strongly proving that our GRPO post-training, guided by robust rewards, learns to handle difficult degradation cases that are challenging to optimize for using L1/L2 loss alone.

F. Additional Visual Results

To further demonstrate the superiority of our proposed method, we provide extensive visual comparisons against state-of-the-art competitors (AirNet [33], PromptIR [49], and AdaIR [10]) on three core restoration tasks: dehazing, denoising, and deraining.

Image Dehazing (Figure 7). As shown in Figure 7, competing methods often suffer from color distortion or residual haze. For instance, in the second row, AirNet and AdaIR fail to completely remove the dense haze in the distance, resulting in low contrast. In contrast, IRPO successfully recovers clear visibility and vibrant colors while maintaining the naturalness of the sky regions, verifying the effectiveness of our *General Reward* in preserving structural fidelity.

Image Denoising (Figure 8). We present results on the challenging $\sigma = 50$ noise level in Figure 8. Severe noise often leads models to over-smooth details. As observed in the "Face" example (fourth row), baselines like PromptIR and AdaIR tend to blur facial features and hair textures. IRPO, guided by our *Task-Aware Reward* (gradient consistency), strikes a better balance between noise removal and texture retention, reconstructing sharper edges and more realistic details.

Image Deraining (Figure 9). Rain streaks often exhibit strong directionality and varying density. In Figure 9, we observe that baselines occasionally leave rain artifacts (first row) or introduce blurring artifacts in background details (third row, fruit stand). Our IRPO leverages the anisotropy consistency reward to effectively distinguish rain streaks from background textures, achieving the cleanest removal performance with minimal artifacts.

Table 7. Comparisons under the three-degradation all-in-one setting: a unified model is trained on a combined set of images obtained from all degradation types and levels. Our model attains a significant average gain of 0.69 dB over AdaIR [10].

Method	Dehazing on SOTS [32]	Deraining on Rain100L [67]	Denoising on BSD68 [46]			Average
			$\sigma = 15$	$\sigma = 25$	$\sigma = 50$	
BRDNet [59]	23.23/0.895	27.42/0.895	32.26/0.898	29.76/0.836	26.34/0.693	27.80/0.843
LPNet [15]	20.84/0.828	24.88/0.784	26.47/0.778	24.77/0.748	21.26/0.552	23.64/0.738
FDGAN [13]	24.71/0.929	29.89/0.933	30.25/0.910	28.81/0.868	26.43/0.776	28.02/0.883
MPRNet [72]	25.28/0.955	33.57/0.954	33.54/0.927	30.89/0.880	27.56/0.779	30.17/0.899
DL [14]	26.92/0.931	32.62/0.931	33.05/0.914	30.41/0.861	26.90/0.740	29.98/0.876
AirNet [33]	27.94/0.962	34.90/0.968	33.92/0.933	31.26/0.888	28.00/0.797	31.20/0.910
PromptIR [49]	30.58/0.974	36.37/0.972	33.98/0.933	31.31/0.888	28.06/0.799	32.06/0.913
AdaIR [10]	31.06/0.980	38.64/0.983	34.12/0.935	31.45/0.892	28.19/0.802	32.69/0.918
IRPO (Ours)	31.62/0.983	39.13/0.988	34.54/0.938	32.04/0.905	29.56/0.823	33.38/0.927

These qualitative comparisons consistently align with our quantitative results, confirming that our data-oriented and reward-oriented paradigm enables the model to generate perceptually superior outcomes across diverse degradations.



Figure 7. Supplementary visual comparisons for image dehazing on synthetic datasets. Our method (IRPO) achieves the highest PSNR scores.



Figure 8. Supplementary visual comparisons for image denoising (noise level 50) on synthetic datasets. Our method (IRPO) consistently recovers finer details.

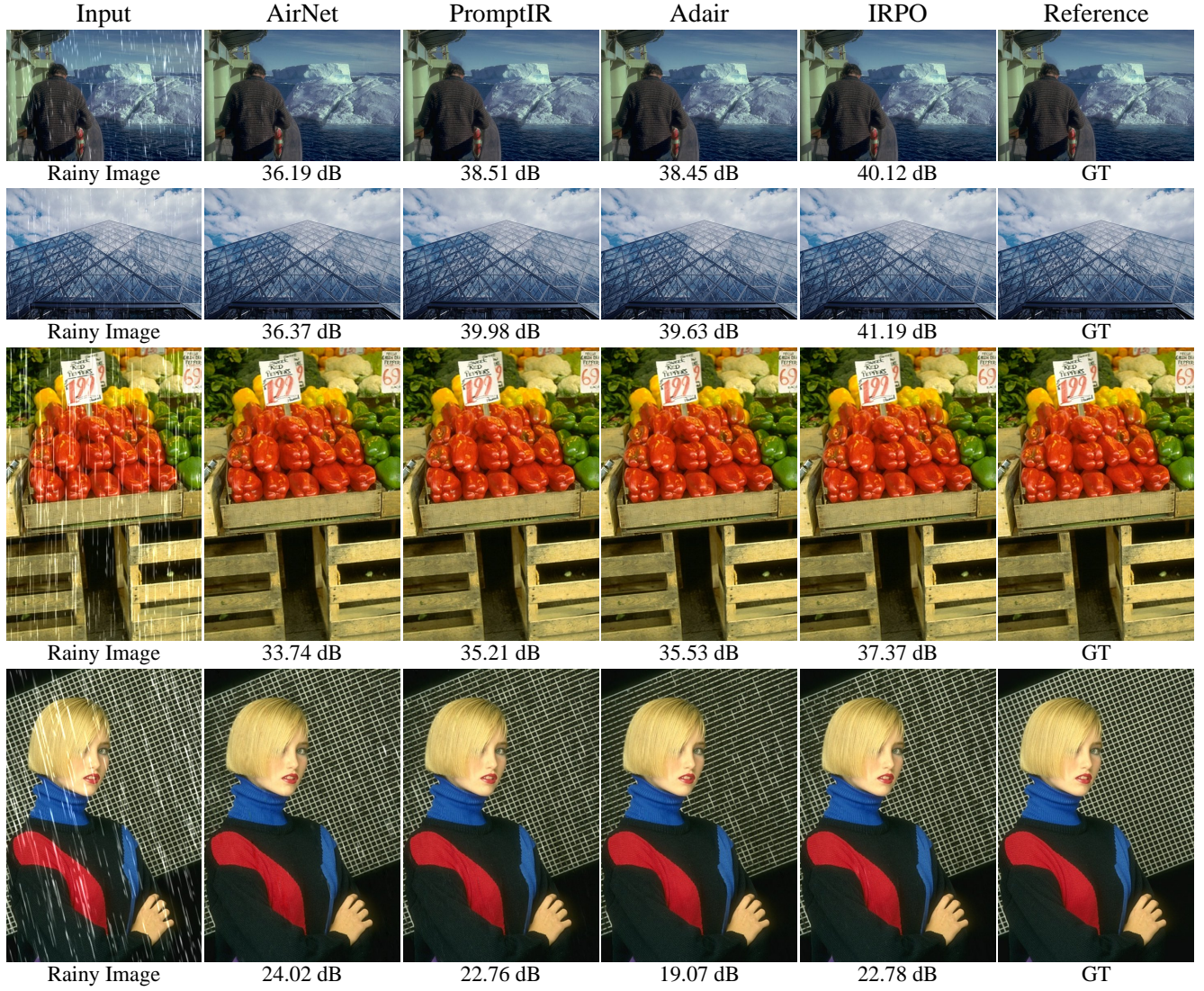


Figure 9. Supplementary visual comparisons for image deraining on synthetic datasets. IRPO achieves superior restoration quality.